

# PHASE FIELD FRACTURE OVER QUADTREES USING THE VIRTUAL ELEMENT METHOD

I. Chryssikou, S. P. Triantafyllou

National Technical University of Athens, Greece, Institute of Structural Analysis and Aseismic Research,  
School of Civil Engineering  
Iroon Polytechniou 9, 15772, Athens, Greece  
e-mail: {chryssikou\_ioulia,savtri}@mail.ntua.gr,

**Key words:** Phase Field Fracture, Quadtree, Adaptive Mesh Refinement, Virtual Element Method

**Abstract.** Predictive modelling of fracture in materials is critical for understanding progressive failure at the material or structure scale. Traditional fracture modeling techniques often require laborious algorithms to track propagating cracks. Conversely, the phase field method has been established as an appealing alternative, mainly due to its favorable implementational features. Yet, criticism to the phase field method involves its ability to accurately resolve crack nucleation and its associated computational costs. In this work, we integrate adaptive quadtree meshing with the Virtual Element Method with the objective of significantly reducing the computational costs of phase field simulations. Quadtree meshing is a hierarchical grid-based technique used for adaptive mesh refinement in 2D simulations. Using the VEM, hanging nodes in the quadtree decomposition are naturally treated and a conforming mesh is always established in contrast to conventional methods. This optimizes computational resources by refining the mesh locally, improving accuracy in complex regions while maintaining coarser elements elsewhere. Different adaptivity criteria are explored and benchmarks pertaining to mode I and mode II brittle fracture are examined in terms of accuracy and efficiency when compared to the standard finite element method.

## 1 INTRODUCTION

Over the past decade, phase field models (PFMs) for fracture have made significant advancements and have been successfully validated in addressing a wide range of complex damage and fracture issues in both brittle and ductile materials. PFMs, a type of variational fracture model, emerged in the mechanics field from the linear elastic principle introduced by Francfort and Marigo [6]. This principle asserts that the actual crack path minimizes the total potential energy, effectively overcoming the limitations of Griffith's energy theory, which required the presence of a pre-existing crack with a clearly defined path.

PFM emerged from the pioneering work of

[6] who proposed a variational theory of fracture based on energy minimization principles. [5] provided a regularised formulation by introducing a length scale parameter that rendered the approach more suitable for numerical approximations. The variational formulation was further modified and extended to multi-dimensional mixed-mode dynamic brittle fractures [12, 17] also targeting the response of high performance composites [9, 19, 21]. The PFM for brittle fracture has been implemented in the commercial software Abaqus [20] via a User Element subroutine by Msekh et al. [18], which was later extended by Liu et al. [15]. Li et al. [14] (see, also, [13]) combined the variational phase field model of brittle fracture with an ex-

tended Cahn-Hilliard model [1, 25], and formulated a fourth-order phase field model suitable resolving crack propagation in anisotropic materials. Rate-dependent PFM models for modelling fracture in visco-elastic solids [23] have also been established. The PFM has found application in the simulation of fractures in plates and shells [2, 11, 22], which involve a 3-D degradation of induced stresses whereas the element kinematics and damage are defined at the mid-surface. Attempts to experimentally validate the method have also been made [see, e.g., 4].

However, the Phase Field Method often requires fine meshes to capture localized features such as sharp interfaces or fracture tips, leading to high computational costs. Adaptive Mesh Refinement (AMR) offers a way to address this issue by dynamically refining the mesh where necessary while maintaining a coarser grid elsewhere, thereby reducing computational effort while preserving accuracy. Some AMR criteria are based directly on the physical characteristics of the problem being solved, such as Energy based criteria and threshold criteria, see, e.g. [7, 8, 10].

In this work, we develop a mesh adaptivity scheme for the Virtual Element Method leveraging the computational merits of quad-tree decompositions [24]. The hanging nodes that arise during adaptivity are naturally treated within the VEM since the resulting elements are polygons. To further speed up the process, we pre-compute state matrices for a family of element patterns. Then during the adaptivity process, these are scaled according to the ratio of the area of each element to the corresponding element from the pre-computed family. Furthermore, a comparison is performed between the VEM and the Scaled Boundary Finite Element method for the case of brittle fracture.

### 1.1 Phase Field for brittle fracture

In the following derivations, the case of the elastic domain  $\Omega$  shown in Fig. 1 is considered. The domain is subjected to body forces  $\mathbf{b}$ , a traction vector  $\bar{\mathbf{t}}$  along  $\partial\Omega_s$  and is supported

along  $\partial\Omega_b$ . A sharp crack interface  $\Gamma_c$  is also defined.

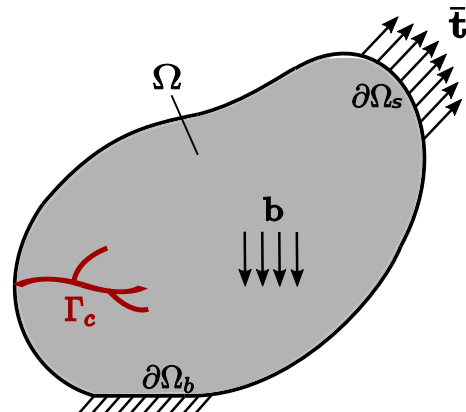


Figure 1: Deformable domain in 2D with sharp crack discontinuity.

The corresponding equilibrium equations are readily defined as

$$\text{Div}(\boldsymbol{\sigma}) + \mathbf{b} = \mathbf{0} \quad (1)$$

where  $\boldsymbol{\sigma}$  is the stress. The domain is considered sufficiently supported to prevent rigid body motion. The phase field method approximates the line integral of the fracture energy, i.e. the energy released due to crack opening along the path  $\Gamma_c$  with a volume integral over the volume of the elastic domain  $\Omega$  according to the following expression

$$\int_{\Gamma_c} G_c dx \approx \int_{\Omega} G_c \left[ \frac{\phi^2}{4l_0} + l_0 \frac{\partial\phi}{\partial x_i} \frac{\partial\phi}{\partial x_j} \right] dx \quad (2)$$

where  $\phi$  is the phase field,  $G_c$  is the critical fracture energy density and  $l_0$  is a length scale. The evolution of the phase field parameter is further governed by the differential equation (3) below

$$\beta\phi - \frac{\partial^2\phi}{\partial x_i^2} = \frac{H}{G_c l_0} \quad (3)$$

where  $i = 1, 2$ ,  $\beta = \left( \frac{H}{G_c l_0} + \frac{1}{4l_0^2} \right)$  and  $H$  is a history field satisfying the following Kuhn-Tucker conditions

$$\psi_{el}^+ - H \leq 0 \quad \dot{H} \geq 0 \quad \dot{H} (\psi_{el}^+ - H) = 0 \quad (4)$$

Equations (4) essentially enforce the irreversibility condition of the crack problem when

no healing mechanisms exist. In equations (4),  $\psi_{el}^+$  denotes the elastic energy density corresponding to the positive components of the strain tensor. This is conveniently evaluated through a polar decomposition of the stress and strain tensor. Further information can be found in Miehe et al. [2]. Within this setting, the elastic energy density is additively decomposed as

$$\psi_{el} = (1 - \phi)^2 \psi_{el}^+ + \psi_{el}^- \quad (5)$$

where  $\psi_{el}^-$  is the elastic energy corresponding to the negative part of the stress and strain tensor (see, e.g., [17]). Equation (5) essentially establishes that (i) decreasing values of  $\phi$  result in a degrading material response;  $\phi = 1$  being a limit value where no degradation takes place and (ii) this degrading behaviour is imposed only on the positive part of the energy density, thus allowing crack propagation due to tensile stresses only.

Equations (1) and (3) form a coupled system of differential equations. Coupling is introduced at the constitutive material level, through consideration of the effect of the phase field on the positive elastic density (equation (5)) and the Kuhn-Tucker conditions introduced in equation (4). Herein, the coupled system is solved by reverting to the Virtual Element Method.

## 2 The Virtual Element Method

The Virtual Element Method has emerged as a promising discretisation approach that generalizes the standard finite element domain decomposition to polygonal (or polyhedral in 3D) elements with any number of edges, also including the the case of non-convex elements. In the case of order 1 VEM, a virtual element el is defined by its corner vertices  $i = 1 \dots v_{el}$ . The edges are denoted by  $e_j$  for  $j = 1, 2, \dots, N_e$  where  $N_e$  is the total number of edges, which is equal to the total number of vertices. Each edge  $e_j$  connects vertices  $v_j$  and  $v_{j+1}$ . The normal vector to the edge is denoted by  $n_i$ . A virtual element comprising 5 nodes is shown in Fig. 2.

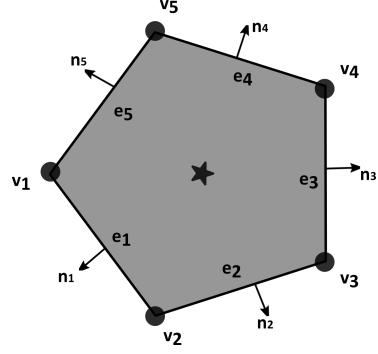


Figure 2: A polygonal virtual element with  $n_e = 5$  edges and  $n = 5$  nodes.

### 2.1 Construction of element state matrices

In the following, only a brief description of the VEM derivations adopted in this work is presented with the objective of highlighting key aspects of the implementation. For the explicit definitions of all the operators involved, we direct the interested reader to [16]. In our order 1 virtual element implementation the diffusion term of the phase field stiffness matrix  $\mathbf{K}_\phi^E$  is derived as

$$\mathbf{K}_\phi^E \approx \mathbf{K}_{\phi,c}^E + \mathbf{K}_{\phi,s}^E = |E| \mathbf{B}_\phi^T \mathbf{B}_\phi + (\mathbb{I}_{N_e} - \Pi_\phi^\nabla)^T (\mathbb{I}_{N_e} - \Pi_\phi^\nabla), \quad (6)$$

where  $\mathbf{K}_{\phi,c}^E$  and  $\mathbf{K}_{\phi,s}^E$  are the consistency and stability term, respectively,  $E$  is the element area,  $\mathbf{B}_\phi$  is the gradient operator defined in Eq. (7)

$$\mathbf{B}_\phi = \frac{1}{2E} (|e_{N_e}|n_{N_e} + |e_1|n_1), (|e_1|n_1 + |e_2|n_2), \dots (|e_{nv-1}|n_{nv-1} + |e_{N_e}|n_{N_e}), \quad (7)$$

$\mathbb{I}_{N_e}$  is the identity matrix, and  $\Pi_\phi^\nabla$  is the second elliptic projection operator see also [16]. The mass term of the phase field stiffness matrix assumes the following form

$$M_E = |E| \beta (\Pi_{\phi^*}^0)^T H \Pi_{\phi^*}^0, \quad (8)$$

where  $\beta$  is defined in Eq. (3),  $\Pi_{\phi^*}^0$  is the first elliptic projection operator defined in Eq. (9),

$$\Pi_{\phi^*}^\nabla = \Pi_{\phi^*}^0 = \left\{ \frac{1}{n_v} [\mathbf{I}_s - [x_s, y_s] \mathbf{B}_\phi] \right\} \quad (9)$$

and

$$H = \mathbf{p}_\phi(x_c, y_c)^T \mathbf{p}_\phi(x_c, y_c) \quad (10)$$

collects the monomials,  $\mathbf{p}_\phi = [1, x, y]$ , of the mapping evaluated at the centroid of the element.

The equivalent load vector is evaluated as

$$\mathbf{F}_\phi = \int_{\mathbf{E}} [\mathbf{p}_\phi(\mathbf{x}) \mathbf{\Pi}_\phi^0]^T \mathbf{f}_\phi(\mathbf{x}) \, d\mathbf{V}. \quad (11)$$

with load term

$$f_\phi(\mathbf{x}) = \frac{H}{G_{cl_0}} \quad (12)$$

The displacement stiffness matrix  $\mathbf{K}_u^E$  is established in a similar fashion, i.e.,

$$\mathbf{K}_u^E \approx \mathbf{K}_{u,c}^E + \mathbf{K}_{u,s}^E = |E| \bar{\mathbf{B}}_u^T \mathbb{C} \bar{\mathbf{B}}_u + (\mathbb{I}_{2N_e} - \mathbf{\Pi}_\phi^\nabla)^T \mathbb{S}_e (\mathbb{I}_{2N_e} - \mathbf{\Pi}_\phi^\nabla), \quad (13)$$

where the gradient operator  $\bar{\mathbf{B}}_u$  is a  $3 \times 2N_e$  defined as

$$\bar{\mathbf{B}}_u = \sum_{\alpha=1}^2 [\mathbf{B}_\phi]_\alpha \otimes \mathcal{N}_\alpha. \quad (14)$$

the term  $[\mathbf{B}_\phi]_\alpha$  corresponds to the  $\alpha^{th}$  row of  $\mathbf{B}_\phi$  and  $\mathcal{N}_1, \mathcal{N}_2$  assume the following form

$$\mathcal{N}_1 = \begin{bmatrix} 1 & 0 \\ 0 & 0 \\ 0 & 1 \end{bmatrix} \quad \mathcal{N}_2 = \begin{bmatrix} 0 & 0 \\ 0 & 1 \\ 1 & 0 \end{bmatrix}. \quad (15)$$

Finally, the term  $\mathbb{S}_e$  in the definition of the stability part in Eq. (13) is defined as, i.e.,

$$\mathbb{S}_e = \max(I_{2N_e}, I_{2N_e} \odot (\mathbf{1}_{2N_e} \otimes \beta \text{diag}(\mathbf{K}_{u,c}^E))), \quad (16)$$

where  $\beta$  is a scaling parameter. All numerical tests in this work have been performed with  $\beta = 0.4$ .

## 2.2 Virtual elements over quad-trees

Quadtree decomposition is a commonly used method for generating structured meshes in two dimensions, particularly for problems that require localized refinement. This approach ensures a smooth transition from a coarse mesh to a finer one while preserving accuracy. Refinement is performed by recursively dividing a rectangular domain (level 1) into four equal

quadrants (level 2), creating a hierarchical mesh structure that leads to progressively finer resolution. In each level of decomposition of the domain, new nodes that come up are called hanging nodes, so the elements with the additional ones can be treated as polygons. This is a huge advantage of the virtual element method.

The element matrices of the master cells are computed and pre-stored in a library. Before the analysis starts, the displacement field, phase field and history variable are set to  $u_0, \phi_0$ , and  $H_0^+$ , respectively. These variables then, are calculated in every step of the simulation. The history variable is calculated based on the strain distribution.

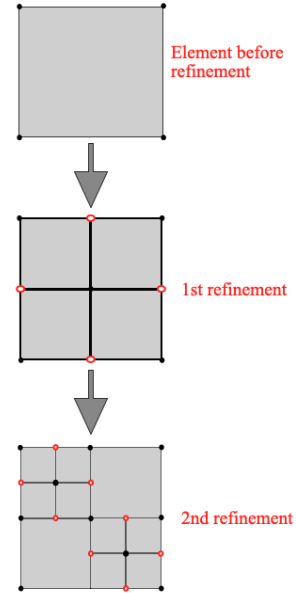


Figure 3: Refinement process using the Quadtree decomposition

With the evolution of the crack, the demand for memory space is increasing in order to store element matrices. Based on the fact that all state matrices are proportional to the area of the element, in this work, we pre-compute them for a family of quadtree elements. These patterns of quadtrees include different types of arrangements of the hanging nodes in an element. Then, the calculation for elements of different sizes that emerge during mesh adaptivity are evaluated by scaling can be done by scaling the

matrices of the 'parent' cell.

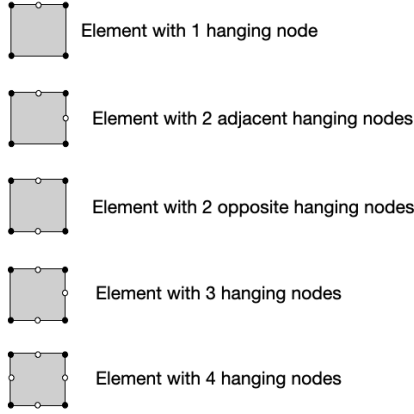


Figure 4: Different patterns of master cells.

### 2.3 Adaptive Refinement criteria

The adaptive mesh refinement strategy employed is based on a dual criterion. At a first level, elements are marked for refinement if their phase field exceeds a threshold value. This threshold is set at 0.6 in this work. At a second level, elements are filtered based on their history variable defined in Eq. (4).

This ensures that the phase field  $\phi$  evolves according to the actual crack driving force. Following closely the methodology proposed in [26], in this work the elements are refined based on the maximum value of the history variable  $h_{max}$ , i.e, whenever the following relation holds

$$\alpha = \frac{\frac{|h^+|}{A_e}}{\sum_{i=1}^{n_v} \frac{h^+}{A_e}} \geq \frac{3G_c}{8l_o}, \quad (17)$$

where  $\alpha$  corresponds to an energy density measure and  $n_v$  is the total number of elements in the current mesh. This condition is evaluated in each incremental step. To avoid over-refining the domain the refinement process terminates as soon as the element size equal half the length scale  $l_o$ .

## 3 Applications

In this section, we evaluate the newly developed adaptive refinement criteria for the phase-field method (PFM) by applying it to three standard benchmark problems. The results obtained

using the proposed approach are compared with those reported in the literature for uniform refinement. For all numerical examples, a state of plane strain is assumed. In all cases, a coarse element discretization is initially considered and a structured quad-tree mesh is generated around the crack. All analyses were performed using an in-house Matlab code and were run on a laptop fitted with an M2 processor and 8GB of RAM.

### 3.1 Tension test

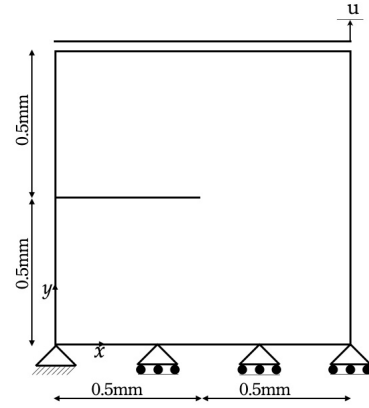


Figure 5: Geometry and boundary conditions of the tension test specimen

The case of a rectangular plate under tension is considered. The geometry and boundary conditions of the specimen are shown in Fig. 5. The bottom edge of the specimen is constrained and the top edge is loaded with uniform displacement  $\Delta_u = 1 \times 10^{-6}$  along the  $y$ -direction, simulating mode-I fracture. The material parameters are  $E = 210kN/mm^2$ ,  $\nu = 0.3$ , the length scale parameter  $l_o = 0.0075mm$  and fracture energy density  $G_c = 0.0027kN/mm^2$ . Plane strain conditions are considered. The total displacement applied in the top edge of the specimen until failure is  $u_{max} = 0.0063mm$  in 6300 time steps.

The obtained results (VEM and SBFEM) are compared with the Scale Boundary Finite Element Method (SBFEM) with adaptive mesh refinement and Virtual Element Method with fine mesh including elements of size  $l_o = 0.02mm$ . The load displacement curve for all methods is presented in Fig. 6 and shows a critical load

before failure  $P_{cr} = 0.688kN$  and a maximum displacement of  $u_{cr} = 0.00562mm$  for VEM with adaptive mesh.

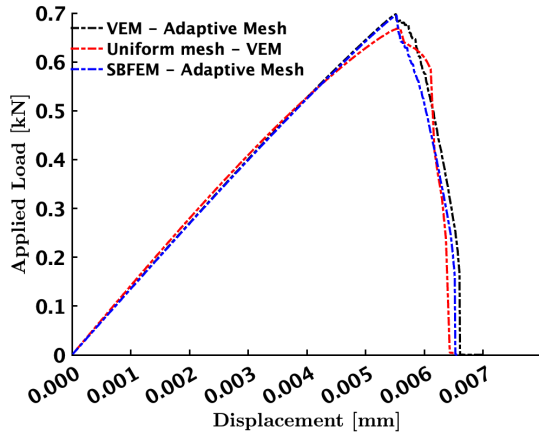


Figure 6: Tension test: Force displacement plots.

All methods seem to perform in a similar manner, but adaptive models tend to have almost identical values for the critical parameters. The deviation between the adaptive SBFEM and VEM cases is 0.7% for the critical force, while the maximum deviation is 1.45% for critical force and 3.77% for displacement. All results are presented in Table 1.

In Figs. 7 and 8, the adaptive mesh and the phase field at the ultimate displacement are shown, respectively, for the case of VEM. Total amount of time for VEM and SBFEM is 180 and 170 minutes respectively.

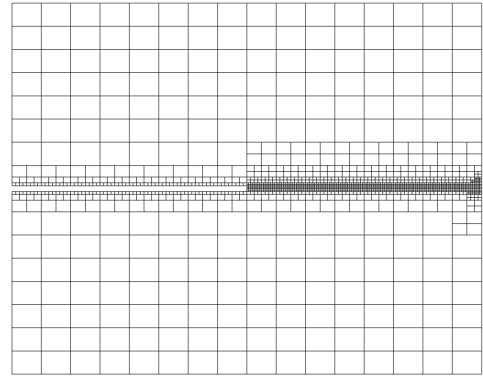


Figure 7: Tension test: Adaptively refined mesh at the final step of the VEM analysis.

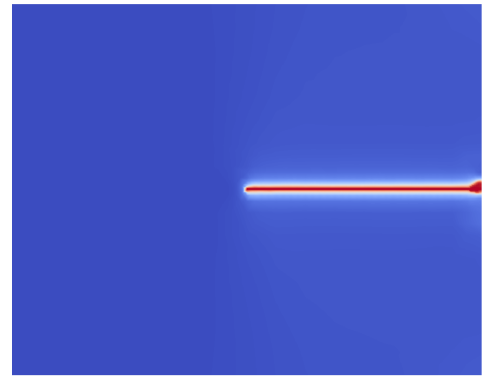


Figure 8: Tension test Phase field at the final step of the adaptive VEM analysis.

Table 1: Tension test: Comparison of key output parameters.

Method	$u_{cr}$ (mm)	$F_{cr}$ (kN)
VEM	0.00552	0.690
SBFEM	0.00551	0.681
Uniform Mesh	0.00559	0.662
Maximum Deviation(%)	1.450	4.000

### 3.2 Shear test

The example of pure shear has been also investigated in many papers from the literature,

see, e.g., [3, 17]. The geometry and boundary conditions are shown in Fig. 9. The displacement increment  $\Delta_u = 10^{-5}mm$  is applied at the top edge along the x-direction. The length scale parameter  $l_o$  is 0.0075mm. As maximum displacement  $U_{max}$ , we consider 0.02mm, to perform the simulation in 2000 steps.

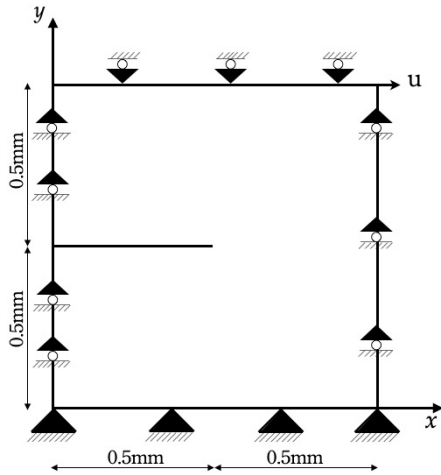


Figure 9: Shear test: Geometry and boundary conditions.

Compared to the tension test, higher deviations are observed in this case, although these are still lower than 5%. More specifically, the critical displacement is 0.0104mm for the adaptive VEM and 0.00995mm for the uniform mesh, which again results in a more conservative estimate. The deviation between the VEM and the SBFEM is practically negligible.

Both the adaptive VEM and SBFEM result in an identical crack path. The computational time for  $\Delta_u = 10^{-5}mm$  was 31 minutes and the number of elements in the simulation was 4613 elements.

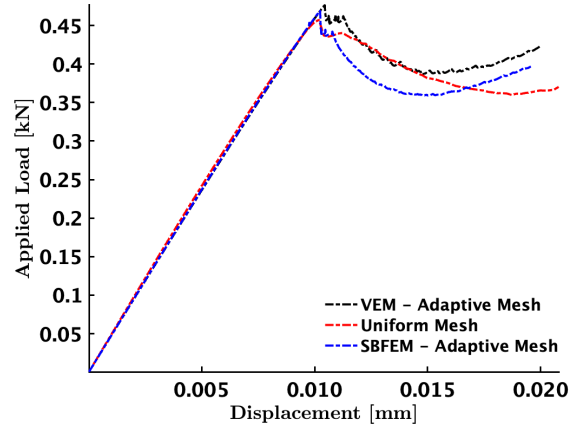


Figure 10: Shear test: Force displacement plots.

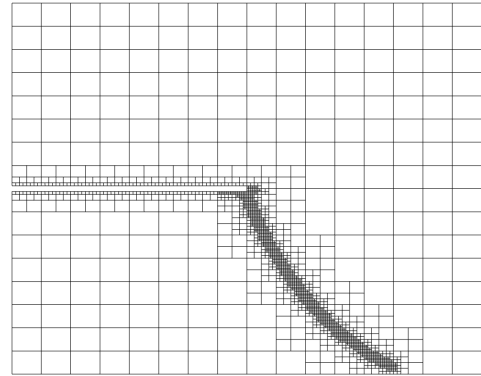


Figure 11: Shear test: adaptive mesh at the ultimate displacement for the VEM.

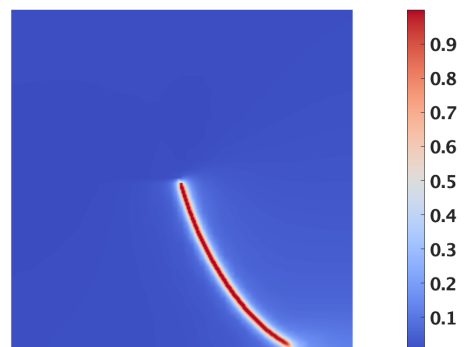


Figure 12: Shear test; Phase field at the final step of the adaptive VEM analysis.

Table 2: Shear test: Comparison of key output parameters.

Method	$u_{cr}$ (mm)	$F_{cr}$ (kN)
VEM	0.01040	0.477
SBFEM	0.01020	0.466
Uniform Mesh	0.00995	0.458
Maximum Deviation(%)	4.300	3.900

### 3.3 L shaped panel test

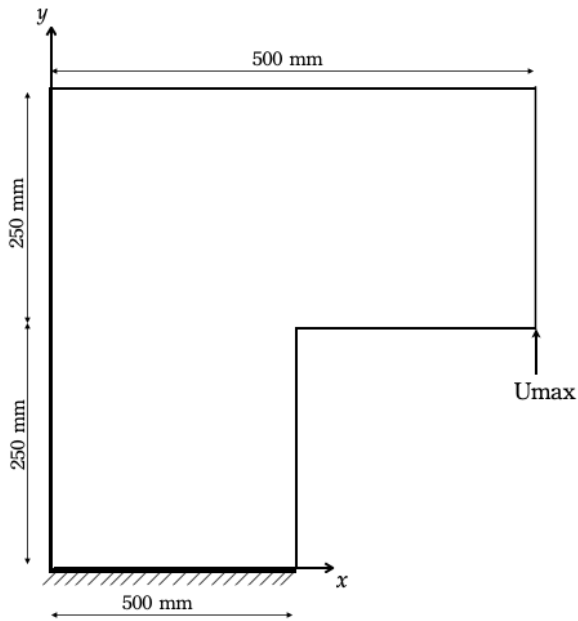


Figure 13: Geometry and boundary conditions for the concrete L shaped panel test

This case has also been extensively examined in the literature, see, e.g., [3] and involves a concrete L-shaped panel subjected to shear loading. The material parameters are  $E = 25.85 \text{ kN/mm}^2$ ,  $\nu = 0.18$ . The simulation is carried out for  $l_o = 1 \text{ mm}, 2.5 \text{ mm}, 5 \text{ mm}$  and  $7.5 \text{ mm}$ . The energy density of the fracture is  $G_c = 8.9 \times 10^{-5} \text{ kN/mm}^2$ . The displacement is controlled at the bottom node of the right edge of the panel as shown in Fig. 13 with an increment of  $\Delta_u = 1e^{-3} \text{ mm}$ . Maximum displacement  $U_{max}$  is 0.9mm and performed in 900 incremental steps. The imposed displacement is reversed at 0.3mm until the value of -0.2mm when a follow-up reversal is performed.

It is important to highlight the fact that upon reversal for the first time, the crack phase is under compression and therefore the crack arrests. One should hence anticipate that the adaptive mesh refinement procedure will also pause.

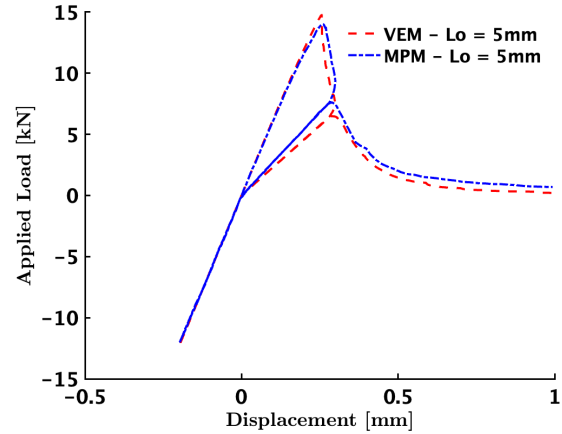


Figure 14: Load-displacement curve and comparison to the literature.

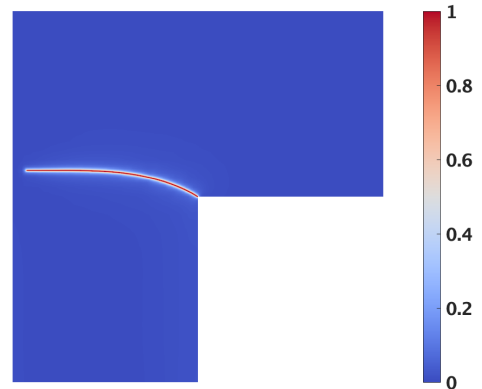


Figure 15: L-panel test; Phase field at the final step of the adaptive VEM analysis.

In Figs. 15 and 16, the phase field at the final step of the analysis and the corresponding adaptive mesh are shown.

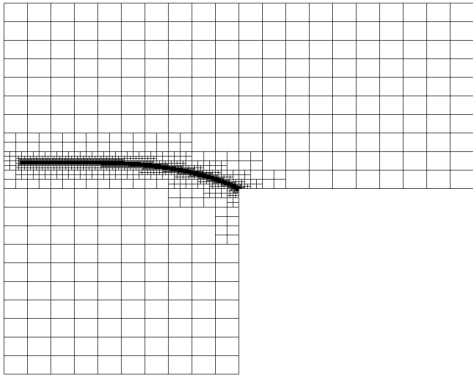
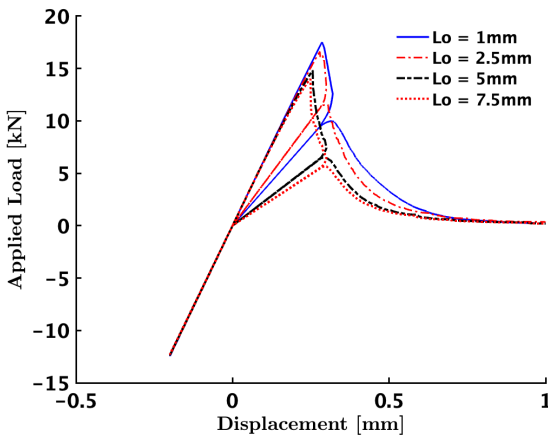


Figure 16: Adaptive Mesh Refinement

Figure 17: Effect of the length scale parameter  $L_o$  in the simulation.

In Fig. 17, the effect of the length scale is shown. Higher values of  $l_o$  result in a broader zone on which the crack diffuses and hence a lower estimate for the peak load of the specimen.

#### 4 CONCLUSIONS

This study aims to explore the benefits of the Phase Field modeling of fracture, when combined with the Virtual Element Method and the newly developed adaptive mesh refinement (AMR) method to study brittle fracture in materials. The AMR method uses Quadtree decomposition of the elements in order to create a path that has a fine mesh to track each crack. This reduces drastically the amount of time needed

for simulations and also does not need the same amount of space as other techniques. The Virtual Element Method has the advantage of treating hanging nodes that appear during the simulation as polygons, making the method more versatile to combine with others. The combination of the two methods makes the code more efficient and flexible with different types of elements. The performance of the proposed framework is validated by several benchmark problems on different choices of mesh.

Future work would be to explore the possibility of simulating dynamic fracture with the proposed framework. Also, the reduction of the computational effort is important, hence the adaptive refinement can be more precise in order to achieve that.

#### Acknowledgements

The research project is implemented in the framework of H.F.R.I call “Basic research Financing (Horizontal support of all Sciences)” under the National Recovery and Resilience Plan “Greece 2.0” funded by the European Union –NextGenerationEU(H.F.R.I. Project Number: 15097). The authors further extend their gratitude to Prof. Chongmin Song and PhD candidate Mr. Hongzhe Chen of the School of Civil and Environmental Engineering, UNSW for providing the SBFEM code that was used as a basis for the developments presented in this work.

#### References

- [1] T. Abinandanan and F. Haider. An extended cahn-hilliard model for interfaces with cubic anisotropy. *Philosophical Magazine A*, 81(10):2457–2479, 2001.
- [2] M. Ambati and L. De Lorenzis. Phase-field modeling of brittle and ductile fracture in shells with isogeometric nurbs-based solid-shell elements. *Computer Methods in Applied Mechanics and Engineering*, 312:351–373, 2016.
- [3] M. Ambati, T. Gerasimov, and L. De Lorenzis. A review on phase-

- field models of brittle fracture and a new fast hybrid formulation. *Computational Mechanics*, 55:383–405, 2015.
- [4] M. Ambati, R. Kruse, and L. De Lorenzis. A phase-field model for ductile fracture at finite strains and its experimental verification. *Computational Mechanics*, 57(1):149–167, 2016.
- [5] B. Bourdin, G. A. Francfort, and J.-J. Marigo. Numerical experiments in revisited brittle fracture. *Journal of the Mechanics and Physics of Solids*, 48(4):797–826, 2000.
- [6] G. A. Francfort and J.-J. Marigo. Revisiting brittle fracture as an energy minimization problem. *Journal of the Mechanics and Physics of Solids*, 46(8):1319–1342, 1998.
- [7] F. Freddi and L. Mingazzi. Adaptive mesh refinement for the phase field method: A fenics implementation. *Applications in Engineering Science*, 14:100127, 2023.
- [8] A. Gupta, U. M. Krishnan, T. K. Mandal, R. Chowdhury, and V. P. Nguyen. An adaptive mesh refinement algorithm for phase-field fracture models: Application to brittle, cohesive, and dynamic fracture. *Computer Methods in Applied Mechanics and Engineering*, 399:115347, 2022.
- [9] A. C. Hansen-Dörr, R. de Borst, P. Henning, and M. Kästner. Phase-field modelling of interface failure in brittle materials. *Computer Methods in Applied Mechanics and Engineering*, 346:25–42, 2019.
- [10] A. Jacon, B. Prabel, G. Molnár, J. Bluthé, and A. Gravouil. Adaptive mesh refinement and cycle jumps for phase-field fatigue fracture modeling. *Finite Elements in Analysis and Design*, 224:104004, 2023.
- [11] J. Kiendl, M. Ambati, L. De Lorenzis, H. Gomez, and A. Reali. Phase-field description of brittle fracture in plates and shells. *Computer Methods in Applied Mechanics and Engineering*, 312:374–394, 2016.
- [12] C. Kuhn and R. Müller. A continuum phase field model for fracture. *Engineering Fracture Mechanics*, 77(18):3625–3634, 2010.
- [13] B. Li and C. Maurini. Crack kinking in a variational phase-field model of brittle fracture with strongly anisotropic surface energy. *Journal of the Mechanics and Physics of Solids*, 2019.
- [14] H. Li, H. Zhang, and Y. Zheng. A coupling extended multiscale finite element method for dynamic analysis of heterogeneous saturated porous media. *International Journal for Numerical Methods in Engineering*, 104(1):18–47, 2015.
- [15] G. Liu, Q. Li, M. A. Msekh, and Z. Zuo. Abaqus implementation of monolithic and staggered schemes for quasi-static and dynamic fracture phase-field model. *Computational Materials Science*, 121:35–47, 2016.
- [16] T.-R. Liu, F. Aldakheel, and M. Aliabadi. Virtual element method for phase field modeling of dynamic fracture. *Computer Methods in Applied Mechanics and Engineering*, 411:116050, 2023.
- [17] C. Miehe, M. Hofacker, and F. Welschinger. A phase field model for rate-independent crack propagation: Robust algorithmic implementation based on operator splits. *Computer Methods in Applied Mechanics and Engineering*, 199(45-48):2765–2778, 2010.
- [18] M. A. Msekh, J. M. Sargado, M. Jamshidian, P. M. Areias, and T. Rabczuk. Abaqus implementation of phase-field model for

- brittle fracture. *Computational Materials Science*, 96:472–484, 2015.
- [19] S. Natarajan, R. K. Annabattula, E. Martínez-Pañeda, et al. Phase field modelling of crack propagation in functionally graded materials. *Composites Part B: Engineering*, 169:239–248, 2019.
- [20] Y. Navidtehrani, C. Betegón, and E. Martínez-Pañeda. A simple and robust abaqus implementation of the phase field fracture method. *Applications in Engineering Science*, 6:100050, 2021.
- [21] A. Quintanas-Corominas, J. Reinoso, E. Casoni, A. Turon, and J. Mayugo. A phase field approach to simulate intralaminar and translaminar fracture in long fiber composite materials. *Composite Structures*, 2019.
- [22] J. Reinoso, M. Paggi, and C. Linder. Phase field modeling of brittle fracture for enhanced assumed strain shells at large deformations: formulation and finite element implementation. *Computational Mechanics*, 59(6):981–1001, 2017.
- [23] R. Shen, H. Waisman, and L. Guo. Fracture of viscoelastic solids modeled with a modified phase field method. *Computer Methods in Applied Mechanics and Engineering*, 346:862–890, 2019.
- [24] A. Tabarraei and N. Sukumar. Adaptive computations on conforming quadtree meshes. *Finite elements in Analysis and Design*, 41(7-8):686–702, 2005.
- [25] S. Torabi and J. Lowengrub. Simulating interfacial anisotropy in thin-film growth using an extended cahn-hilliard model. *Physical Review E*, 85(4):041603, 2012.
- [26] Y. Yu, C. Hou, and M. Zhao. Phase field model for brittle fracture using threshold strategy. *Theoretical and Applied Fracture Mechanics*, 125:103831, 2023. ISSN 0167-8442. doi: <https://doi.org/10.1016/j.tafmec.2023.103831>.